Francis Loth
Associate Professor,
Department of Mechanical Engineering and
Industrial Engineering,
The University of Illinois at Chicago,
Chicago, Illinois, 60607
e-mail: floth@uic.edu

Paul F. Fischer
Research Scientist,
Mathematics and Computer Science Division,
Argonne National Laboratory,
Argonne, Illinois, 60439
e-mail: fischer@mcs.anl.gov

Nurullah Arslan
Assistant Professor,
Department of Industrial Engineering,
Fatih University,
Istanbul, Turkey
e-mail: narslan@fatih.edu.tr

Christopher D. Bertram
Associate Professor,
Graduate School of Biomedical Engineering,
University of New South Wales,
Sydney, Australia, 2033
e-mail: c.bertram@unsw.edu.au

Seung E. Lee
M.S. student,
Department of Mechanical Engineering,
The University of Illinois at Chicago,
Chicago, Illinois, 60607
e-mail: slee48@uic.edu

Thomas J. Royston
Associate Professor,
Department of Mechanical Engineering,
The University of Illinois at Chicago,
Chicago, Illinois, 60607
e-mail: troyston@uic.edu

Wael E. Shaalan
Visiting Research Associate,
Department of Surgery,
The University of Chicago,
Chicago, Illinois, 60637
e-mail: wshaalan@surgery.bsd.uchicago.edu

Hisham S. Bassiouny
Associate Professor,
Department of Surgery,
The University of Chicago,
Chicago, Illinois, 60637
e-mail: hbassiou@surgery.bsd.uchicago.edu

Transitional Flow at the Venous Anastomosis of an Arteriovenous Graft: Potential Activation of the ERK1/2 Mechanotransduction Pathway

We present experimental and computational results that describe the level, distribution, and importance of velocity fluctuations within the venous anastomosis of an arteriovenous graft. The motivation of this work is to understand better the importance of biomechanical forces in the development of intimal hyperplasia within these grafts. Steady-flow in vitro studies (Re=1060 and 1820) were conducted within a graft model that represents the venous anastomosis to measure velocity by means of laser Doppler anemometry. Numerical simulations with the same geometry and flow conditions were conducted by employing the spectral element technique. As flow enters the vein from the graft, the velocity field exhibits flow separation and coherent structures (weak turbulence) that originate from the separation shear layer. We also report results of a porcine animal study in which the distribution and magnitude of vein-wall vibration on the venous anastomosis were measured at the time of graft construction. Preliminary molecular biology studies indicate elevated activity levels of the extracellular regulatory kinase ERK1/2, a mitogen-activated protein kinase involved in mechanotransduction, at regions of increased vein-wall vibration. These findings suggest a potential relationship between the associated turbulence-induced vein-wall vibration and the development of intimal hyperplasia in arteriovenous grafts. Further research is necessary, however, in order to determine if a correlation exists and to differentiate the vibration effect from that of flow related effects.
[DOI: 10.1115/1.1537737]

Introduction

Individuals with end-stage renal disease would succumb within a few weeks or months if not sustained by some form of dialysis therapy or a kidney transplant. For hemodialysis patients, an arteriovenous (AV) graft (Fig. 1) is constructed from an artery to a vein to provide an access site. By bypassing the high-resistance vessels (arterioles and venules), high flow-rates can be achieved that are necessary for efficient hemodialysis. Polytetrafluoroethylene (PTFE), a synthetic graft material, is often used for these grafts. Unfortunately, more than half of the AV grafts fail and require surgical reconstruction within three years [1]. The majority of these graft failures are caused by occlusive venous anasto-

Contributed by the Bioengineering Division for publication in the JOURNAL OF BIOMECHANICAL ENGINEERING. Manuscript received September 2001; revised manuscript received August 2002. Associate Editor: J. E. Moore.

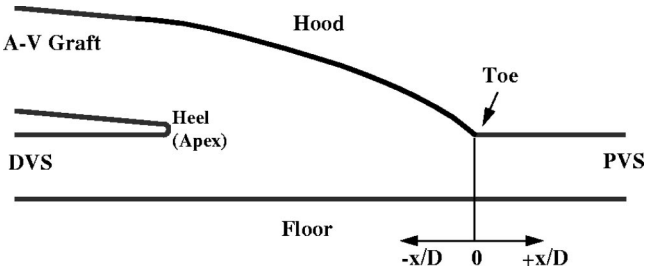

Fig. 1 Geometry and nomenclature of the venous anastomosis A-V graft model

motic intimal hyperplasia (VAIH), which is a stenosis or narrowing of the vein downstream of the graft. Because the use of AV grafts as hemodialysis access grafts is expected to rise, there is significant interest in finding treatments that prevent or reduce the development of VAIH in AV grafts.

While the natural healing response after surgery causes some degree of intimal thickening, the biomechanical environment appears to be responsible for progression of intimal thickening to occlusive VAIH. Biomechanical forces in the AV graft are unique, with generally high wall shear stress (WSS) acting on the vein, a region of flow separation, and pressure fluctuations that vibrate the vein wall and surrounding tissue. Kanterman et al. have shown that hyperplastic stenoses occur predominantly in the proximal venous segment (PVS), downstream of the graft-to-vein junction [1]. This observation suggests the possible involvement of disturbances to flow created in the graft-to-vein junction and advected downstream. In a canine animal model, Fillinger et al. [2–5] measured perivascular tissue vibration and intimal hyperplasia (IH) in AV graft venous anastomoses, to investigate the results of varying both flow-rate and geometric details. They found the highest tissue vibration and IH to be correlated ($r=0.92, p<0.001$) [4]. In the absence of direct measurements of flow turbulence, they hypothesized that tissue vibration was caused by turbulent flow and that the degree of vibration was correlated with the blood turbulence level. They concluded that a high flow-rate in these grafts led to flow disturbances, deposition of vibration energy in the vessel wall, venous intimal-medial thickening, and the initiation of IH.

Extensive numerical and experimental investigations [6–19] of the fluid dynamics of distal end-to-side anastomoses associated with arterial bypass grafts have been conducted, motivated by the fact that this junction is a site of particularly high risk in IH. A further motivation is that the junction offers a situation providing a complex mix of fluid-dynamic phenomena and can potentially aid the quest for causal linkages between disease localization and fluid-dynamic details for arteries in general. The fluid mechanics of the arterial and venous end-to-side anastomoses differ primarily because of differences in flow-rate. This produces a much higher Reynolds number in the graft-to-vein junction than in the distal arterial end-to-side anastomosis and implies a greater tendency to flow instability and turbulence, as noted by Fillinger et al. [3]. In addition, mean pressure is much lower (2–3 times) and overall mean WSS is much greater (5–10 times) in a venous anastomosis compared with the arterial anastomosis. Vein grafts are known to remodel (arterialize) when placed in an arterial circuit due to the increased pressure and WSS environment. Thus, the remodeling process is expected to differ within a venous anastomosis. The differences in hemodynamics and the biological differences in the arterial and venous wall suggest that VAIH in hemodialysis grafts and IH in arterial bypass grafts should be considered as two distinctly different phenomena [3,20].

Shu et al. [21–24] experimentally obtained the mean velocity profiles and WSS inside realistic AV graft models. They implicate the low and oscillating WSS near the stagnation point and separation region in the development of a lesion downstream of the toe. No measurements of turbulence levels were reported. Ethier et al. [6] described separation patterns in a 45° junction that resembles the venous anastomosis at Reynolds numbers in the range 250 to 1650. Transition to unsteadiness was observed experimentally at Re=1650 but not at Re=1100. A recent study by Ene-Iordache et al. [25] examined the fluid dynamics of arteriovenous fistulas using computational fluid dynamics (CFD). The geometry was based on a 3D reconstruction of a patient geometry. While this geometry differs from the end-to-side venous anastomosis, the high flow rate and sharp bend of the radial artery on the venous artery caused the vessel wall to be subjected to high WSS, flow circulation, and areas of elevated WSS gradients with Re values ranging from 658 to 1275. However, they did not report transitional flow. In the present study, we present experimental and numerical results that detail the transitional nature of flow in the venous anastomosis of an AV graft.

The activation of mitogen-activated protein kinases (MAPKs) and cytokines has been demonstrated in response to hemodynamic shear forces in endothelial cells *in vitro*. Both the stimulatory effects of temporal gradients in shear and the inhibitory effects of steady shear on gene expression were found to be mediated by activation and inactivation of immediate early genes (Egr-1, c-jun, c-fos) [26,27]. In other studies, MAPKs including ERK1/2 and JNK have been shown to play an important role in shear-stress-mediated endothelial gene expression [28]. However, the vein-wall MAPK response to varying magnitudes of tensile and shear stress *in vivo* remains largely unknown.

Altered hemodynamics induces an adaptive response of the vessel wall that involves migration and proliferation of vascular smooth muscle cells (VSMCs) in the subintimal space [29]. The cellular mechanisms include the activation of intracellular signalling molecules such as MAPKs [30–32]. The first identified MAPK cascade is composed of the MAPKs ERK1 and ERK2 and has been best characterized as mediating signal transduction by hemodynamic forces and growth factors. Shear-induced ERK1/2 activation was attenuated when endothelial cells were pre-treated with MAPK inhibitors [33]. Upon phosphorylated activation of ERK1/2, nuclear translocation of the complex is critical for early immediate gene expression [34,35]. Specifically, within the nucleus ERK1/2 is responsible for phosphorylation of the nuclear transcription factor Elk-1. By binding to a sequence in the promoter region of Egr-1, Elk-1 has been shown to be an essential component of shear-induced Egr-1 transcriptional activation [36]. We have previously shown that following experimental arterial injury, reduced levels of flow and hemodynamic shear upregulates *in vivo* levels of Egr-1 responsible for the coordinated expression of endothelial and VSMC proteins such as PDGF-A, PDGF-B, and TGF-β [37,38].

The goal of the present research is to investigate the possible relationship between the hemodynamic environment (turbulence and WSS levels) of the AV graft and AV graft failure. We report evidence regarding the level and importance of velocity fluctuations within the venous anastomosis based on (1) color Doppler ultrasound measurements in a human AV graft, (2) experimental measurements of velocity within an *in vitro* model, (3) WSS and velocity simulations using computational fluid dynamics for the same geometry, (4) vein-wall vibration measurements taken during a porcine animal study, and (5) preliminary molecular biological studies regarding the distribution and level of activity of ERK1/2 at different regions of the venous anastomosis.

Methods

Human AV Graft Hemodynamics. Color Doppler ultrasound measurements (Acuson 128XP/10) were conducted to determine AV graft-vein junction flow conditions and vessel diameters on two dialysis patients within one month of graft implantation. The PTFE AV graft connected the brachial artery to the basilic vein in the antecubital fossa. Based on measurements taken from a B-scan-mode outline, the graft lumen diameters (D_g)

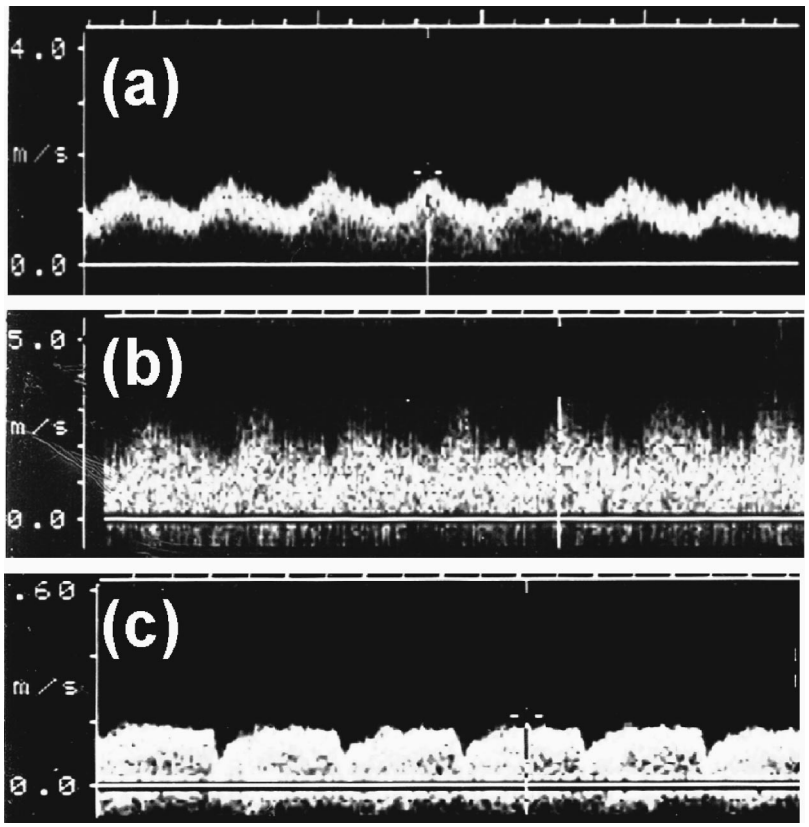

Fig. 2 Color Doppler ultrasound images on a dialysis patient's graft-to-vein junction (venous anastomosis). Velocity traces are shown for measurements taken near the centerline of the (*a*) PTFE graft, (*b*) proximal venous segment (PVS), and (*c*) distal venous segment (DVS). Note the large magnitude of velocities in the graft and PVS with significant spectral broadening in the PVS trace.

were 6.0 and 6.7 mm. In both patients, the proximal and distal venous segments (DVS) were of comparable diameter and somewhat smaller than the graft. The angle between the graft and the vein was approximately 45° in one patient and less than 10° in the other patient. The anastomotic geometry varies considerably from patient to patient for surgical reasons.

After the flow was imaged in color Doppler scan mode, a static Doppler sample volume was deposited in the center of each vessel, spanning approximately one-third of the vessel diameter. A marker was aligned with the vessel axis, and the angle between the Doppler line of sight and the vessel axis was computed. Since the Doppler scan plane was arranged to contain the axes of the vein and the graft at the junction, this measured angle was the true angle between the Doppler line of sight and the vessel axis. It was therefore possible to compute true axial velocities.

The velocity trace for the graft showed much higher velocities than in normal arteries, with a low pulsatility index because the sonograph trace remained well above zero throughout the cycle (Fig. 2*a*). For one patient, the instantaneous mean of the sonograph trace was estimated to be 1.5 m/s at the maximum and 1.0 m/s at the minimum of the cycle. For the other patient, the corresponding numbers were 1.2 and 0.8 m/s. Measurements were also made in the PVS and DVS (Fig. 2*b* & 2*c*); however, determination of the mean velocity was difficult because of the degree of spectral broadening. The significant spectral broadening of the Doppler signal in the PVS is likely due to the transitional nature of the flow within the PVS.

Reynolds numbers for the graft are difficult to estimate because the shape of the velocity profile is unknown and the sample volume does not cover the whole vessel lumen. If one assumes a flat velocity profile and normal blood viscosity and density ($\mu = 3.5$ mPa·s, $\rho = 1050$ kg/m^3), the above measurements lead to a systolic peak Reynolds number of $\mathrm{Re}_g = \rho V_{avg} D_g / \mu = 2700$ and a diastolic minimum of 1800 for one patient. For the other patient, the corresponding values are 2400 and 1600. Under the assumption of a parabolic flow profile, the Reynolds numbers would be half as much. The true *in vivo* Reynolds numbers therefore remain unknown, although they are expected to fall somewhere between values for parabolic and flat velocity profiles. Thus, Reynolds numbers at diastole and systole are estimated as 1100 and 1800, respectively. These Reynolds numbers correspond to flow rates of 1.0 and 1.7 liters/min at diastole and systole, respectively for a graft diameter of 6 mm. These values are similar to those employed in studies by Shu et al. [22–24] and to human *in vivo* values reported in the literature [39]. Flow entering from the DVS was estimated to be 10% of the total blood flow; however, clinical experience is that the DVS sometimes occludes due to thrombus.

Flow Model Geometry. The anastomosis model used in this study was that previously used by Loth et al. [12] to investigate the hemodynamics in a distal end-to-side arterial bypass anastomosis. This model geometry also closely approximates the graft-vein junction of the AV graft. The model was up-scaled 7.6 times relative to the *in vivo* case. The model material was a transparent elastomer (Sylgard 184, Dow Corning), and the walls were thick enough that the model could be considered essentially rigid. The graft-to-vein diameter ratio was 1.6, with a graft lumen diameter of 50.8 mm and a host vein diameter of 31.75 mm. The graft axis intersected the host vein axis at an angle of 5°.

In Vitro Measurements

Flow System. A flow system was designed and constructed to provide the up-scaled model with the proper inlet and outlet flow conditions. A mixture of 42% water and 58% glycerin by weight was chosen to match the index of refraction ($n=1.41$) of the Sylgard model. This fluid had a density of 1110 kg/m^3 and a dynamic viscosity of 10 mPa·s at 23°C, as measured by a spindle-type digital viscometer (Brookfield model LVTDV-II). A 1/3 HP split-phase centrifugal pump (Teel model 1V308) provided the pressure head to drive the flow. A graduated cylinder-and-stopwatch was used to measure the total flow-rate. The ratio of the graft inlet flow-rate to the DVS inlet flow-rate was 9:1. The DVS inlet flow-rate was measured by an ultrasound transit-time flowmeter (Transonic Systems model T101). Since fluid viscosity depends on temperature, a heater/mixer in the downstream tank was used to keep the fluid temperature at 23 ± 0.5°C during the experiments. The model was placed in a flow circuit under steady-flow conditions such that flow entered the graft from a straight tube 4 m long with an inner diameter of 50.8 mm. Two different steady flow-rates were set up, each with the same inlet flow ratio between the graft and the DVS. The corresponding Reynolds numbers based on the graft flow-rate and graft diameter were 1060 and 1820.

Laser Doppler anemometry (LDA) measurements were taken both in the midplane and away from the midplane for the velocity components parallel and perpendicular to the floor (u and v, respectively). For Reynolds number 1060, velocity profiles were measured at 13 axial locations at the midplane. Outside the midplane, velocity profiles were measured along five lines on the graft side at a distance $0.8D$ (D=vein diameter) from the hood-midplane intersection and 11 lines on the vein side $0.5D$ from the floor-midplane intersection. Preliminary measurements revealed that the turbulent fluctuation amplitudes within the anastomotic region (region between the toe and heel) were comparable to or lower than those measured at the AV graft and DVS inlets (X/D $\leqslant -5.2$). On this basis, detailed measurements for the higher Reynolds number were confined to the graft inlet, the furthest proximal axial location within the anastomosis, and the PVS. For Reynolds number 1820, velocity measurements were taken at six axial locations in the midplane and away from the midplane on the vein side $0.5D$ from the floor.

The LDA system (DANTEC Electronics mirror-type F147/B073, Model 5500A) uses two colors (blue=488 nm, green =514.5 nm) to measure two components of velocity. A 350 mW argon-ion laser provided the laser output. The system consists of two Bragg cells, two photomultipliers with receiving optics and two electronic counters. The Bragg cells enable forward and reverse velocities to be distinguished. Back-scattered light coming from the particles in the sample volume is collected at the photomultiplier tube, in which the signal is amplified. The signal was processed by an electronic counter (DANTEC 50N10 signal processor) to obtain the Doppler-shifted frequency. The diameter (d_m) and length (l_m) of the blue-beam ellipsoidal sample volume were 0.19 and 1.66 mm, respectively. The particles used to scatter the laser light were 0.993 μm-diameter polymer microspheres (Duke Scientific Corporation, Palo Alto, CA, no. 4009B). The concentration of particles in the water-glycerin mixture (2.3×10^9 particles/liter) was determined by the ratio of the total volume of liquid in the system to the sample volume such that, on average, only one particle would be in the sample volume at a given time.

The data acquisition program SIZEware was used to record the instantaneous velocity for steady flow. Five thousand validated samples were recorded at each location in the flow field away from the wall, and then the mean velocity was found by taking the averages of the samples for the u and v components of the velocity. Since the data rate was lower near the wall of the model, elapsed time mode was used, and data were taken for five minutes (200–1000 validated samples). The calculations for mean velocities, fluctuation velocities, and Reynolds stress are defined in the following equations:

$$\overline{u}=\frac{\sum_{i=1}^{N}u_i}{N},\quad \overline{v}=\frac{\sum_{i=1}^{N}v_i}{N},\quad \overline{(u')^2}=\frac{\sum_{i=1}^{N}(u_i-\overline{u})^2}{N},$$

$$\overline{(v')^2}=\frac{\sum_{i=1}^{N}(v_i-\overline{v})^2}{N},$$

$$u_{rms}=\sqrt{\overline{(u')^2}},\quad v_{rms}=\sqrt{\overline{(v')^2}},\quad \overline{u'v'}=\frac{\sum_{i=1}^{N}(u_i-\overline{u})(v_i-\overline{v})}{N}.$$

u_i — instantaneous velocity component of ith particle in the x direction
v_i — instantaneous velocity component of ith particle in the y direction
N — number of spherical particles passing through the measurement volume

All data are presented at *in vivo* scale by converting the *in vitro* measurements through dynamic similarity ($\mathrm{Re}=\rho VD_g/\mu$), where the *in vivo* values are $D_g=6.7$ mm, $\rho=1050$ kg/m^3, $\mu=3.5$ mPa·s). Note that the Reynolds number based on the vein diameter differs from that based on the graft diameter by the ratio of the vessel diameters and flow-rates and is given by $\mathrm{Re}_v=(D/D_g)(Q_v/Q_g)\mathrm{Re}=(1.6/0.9)\mathrm{Re}$.

Numerical Simulation

Mesh Development. The mesh generation involved two main steps. First, axial images of the model bifurcation were converted into 3D-lumen geometry in a rapid-prototype file format. Second, the above geometry was used to generate the vertices and connectivity of a CFD mesh. The Sylgard model was imaged axially using a spiral computerized X-ray tomography (CT) scanner (high speed CTI GE) with an axial spacing of 1 mm (256×256 pixels, field of view 120×120 mm). The calculated pixel size was 0.5×0.5 mm and a total of 250 axial images were acquired. The software package Mimics (Materialise, Ann Arbor, MI) was used to view the images and obtain the 3D-lumen geometry. With Mimics, edge detection by thresholding was used to determine the lumen contour for each image. After initial edge detection, images were further refined manually, pixel by pixel, to achieve the (operator-perceived) best description of the lumen geometry (Fig. 3). Points along each contour were unevenly spaced. A FORTRAN code was written to re-interpolate these points to be equidistant along the contour (0.25 mm) and to smooth the surface geometry. The 3D geometric data represented as contour information were used to create a 3D mesh with the topology shown in Fig. 4*a* and *b*. The mesh for the Re=1060 case comprised $K=1968$ hexahedral elements. For the Re=1820 case, the mesh was locally refined in the transitional flow region to yield $K=6168$ elements, as illustrated in Fig. 4*c*. Details of the image reconstruction and mesh generation techniques are given by Yedavalli et al. [40] and Lee et al. [41], respectively.

Solution Technique. The solution technique used a spectral element code developed at Argonne National Laboratory (Illinois, USA) that is designed specifically for simulation of transitional and turbulent flows in complex geometries. The code is based on the spectral element method, which represents velocity and pressure as Nth-order tensor-product polynomials within each of K computational mesh cells (bricks). The total number of grid-points is approximately KN^3. The polynomials can be differentiated to compute derived quantities, such as WSS, and provide for accurate high-Reynolds number solutions with minimal numerical dis-

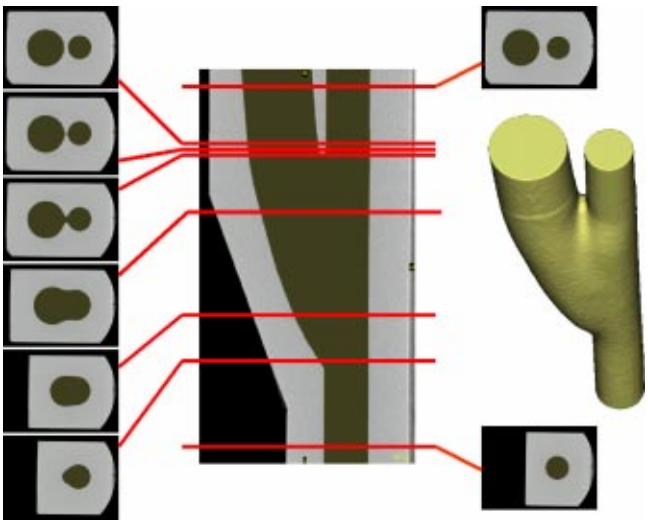

Fig. 3 Computerized tomography images of the AV graft physical model used to measure the 3D lumen geometry

sipation and dispersion. Third-order-accurate time stepping was employed, and the solution was stabilized by using the filter described by Fischer and Mullen [42]. Temporal and spatial convergence results have been presented previously [43]. Further details of the discretization and solution method are given by Fischer et al. [44].

Fully developed Poiseuille flow was imposed at the graft and vein (DVS) inlets, and stress-free boundary conditions were imposed at the PVS outlet. Blood was approximated as a Newtonian fluid and the venous anastomosis was assumed to be rigid. The present calculations were conducted with $N=7$. Short-time numerical convergence studies at $N=9$ and $N=11$ confirmed the adequacy of the spatial resolution. The simulations were initiated at Re=60 and smoothly ramped to Re=1060 by reducing the viscosity. The solution was then interpolated onto the $K=6168$ mesh and ramped to Re=1820. The flow field downstream of the toe became unsteady, with periodic shedding of coherent structures (hairpin vortices). The initial conditions were flushed through the domain prior to accumulation of statistics, which were taken over a 0.04 s interval corresponding to roughly 28 vortex shedding cycles. This simulation required roughly 14,000 time-steps and about 5 days of computing time on 32 processors of the SGI Origin2000 at Argonne National Laboratory.

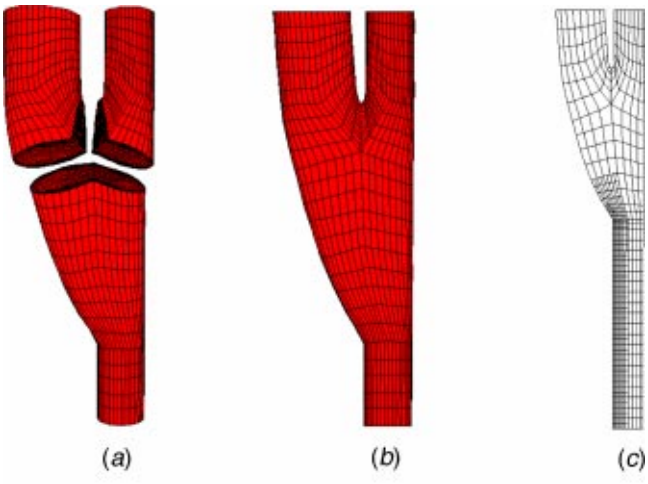

Fig. 4 Three curved tubes with two angled surfaces (*a*) are joined to create the 3-D bifurcation representing the arterio-venous geometry (*b*). This mesh is refined and extensions are added to produce the final mesh (*c*).

Porcine AV Graft Model

Animal Model. Three male miniature swine (25–30 kg) fed normal pig chow were used for the study. Anesthesia was induced by intramuscular injection of ketamine hydrochloride (2.2 mg/kg), xylazine (2.2 mg/kg), telazol (4.4 mg/kg), and atropine (0.4 mg/kg) and was maintained with 1–2.5% isoflurane via endotracheal intubation. To reduce the incidence of graft thrombosis, all animals were given 80 mg of aspirin orally one day preoperatively and postoperatively for the duration of the selected time course. Heparin sulfate (100 IU/kg) was administered intravenously 5 minutes prior to implantation of the infrarenal aorta-to-external-iliac-vein AV grafts to minimize perioperative graft thrombosis. Animals were killed by a lethal intravascular injection of sodium pentobarbital under general anesthesia following intervention. Housing and handling of animals were compliant with ''Principles of Laboratory Animal Care'' and ''Guide for the Care and Use of Laboratory Animals'' (NIH publication #80-23, revised 1985).

The aorta-to-external-iliac-vein graft implantation was performed as follows. By means of a retroperitoneal right flank incision, the parietal peritoneum was reflected off the iliopsoas muscle. The distal infrarenal aorta and external iliac vein were dissected. The internal iliac vein was ligated at its confluence to create a relatively generous proximal outflow segment with no side branches such that the turbulent flow field properties were not influenced by convergence or mixing of blood flow. A 4–7 mm externally reinforced PTFE graft was anastomosed proximally to the partially side-clamped aorta in an end-to-side fashion with 6/0 prolene suture. The graft was positioned in the retroperitoneal space by using a loop configuration. The external iliac vein was subsequently controlled with atraumatic clamps remote from the planned anastomotic site. A longitudinal venotomy was created by using a #11 knife along the anterolateral aspect and extended to a length equal to 1.5 vein diameters. The 7 mm end of the graft was trimmed to the length of the venotomy and anastomosed in an end-to-side fashion with 6/0 prolene suture. After flushing any potential air or debris, the aortic and venous clamps were released. The constructed graft geometry is sketched in Fig. 5.

Vein-Wall Vibration Measurements. Non-contacting measurements of radial vein surface motion (vibration velocity) were made by using laser Doppler vibrometry (LDV, Polytec CLV-800) on each porcine AV graft vein anastomosis on the porcine animal model on the exposed lateral wall at three regions indicated in Fig. 5. Similar measurements have been reported in the literature [45,46] on a soft tissue phantom. The measured velocity levels were several orders of magnitude larger than the threshold sensitivity of the LDV (0.3 μm/s). Vein-wall vibration velocity was recorded at a sample rate of 2048 Hz for 4 s using a dynamic FFT signal analyzer (Hewlett Packard model 35670). Due to the Nyquist criterion and necessary signal conditioning, this yielded measurements of vibratory motion up to 800 Hz with a frequency resolution of 0.25 Hz. Pressure during the cardiac cycle was also measured with a high fidelity pressure catheter (Millar Instruments Inc., Micro-tip Catheter Transducer, Model SPR-524, 3F) introduced via the distal external iliac venous segment. In addition, pulsatile blood flow rate in the proximal AV graft vein was measured by a transit time flow meter (Transonic Inc.).

Molecular Biology. Frozen tissue from the vein segment was homogenized with a Polytron PCU-2-110 homogenizer (Kinematica) on ice in the lysis buffer containing 50 mM Tris (Ph 7.6), 0.5% Triton X-100, 150 mM NaCl, 5 mM EDTA, 1 mM Na_3VO_4, 10 μg/ml leupeptin, 10 μg/ml aprotinin, 25 mM p-nitrophenyl p′-guanidino-benzoate, 1 mM PMSF, 1 mM NaF, 10 μg/ml trypsin inhibitor, 1 mM benzamidine. The homogenate was incu-

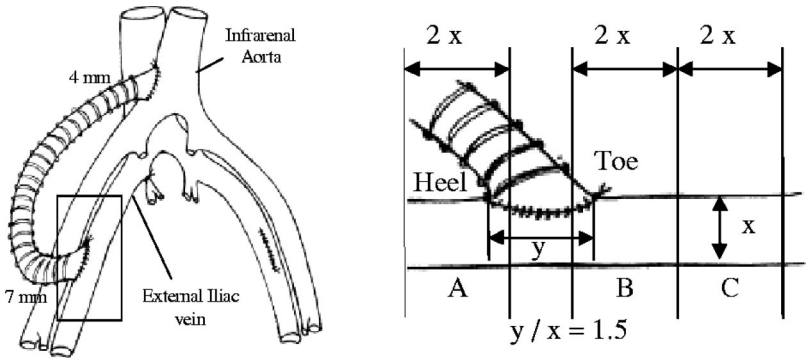

Fig. 5 Sketch of the aorto-external iliac vein graft (LEFT) and the anastomotic geometry with defined regions for biomechanical and biologic studies (RIGHT)

bated on ice for 15 min and centrifuged at 14,000 g for 30 min. The supernatant was harvested, and protein concentration was measured by the Bradford method.

Western blot analysis was performed on one animal 4 hours after graft creation to measure protein levels of ERK1/2 and JNK in the extracts of porcine grafts. The protein extracts (40 μg/lane) were heated at 95°C for 5 min in a sample buffer (94 mM phosphate buffer pH 7.0, 1% SDS, 2 M urea, and 3% β-ME); electrophoresis then was performed on 10% SDS-PAGE under reducing conditions. The gels were placed onto Immobilon-P sheets (Millipore, Bedford, MA) that previously had been wetted with a buffer containing 25 mM Tris and 39 mM glycine, pH 8.9. Blotting was performed on a horizontal semi-dry electroblot apparatus (Pharmacia-LKB, Piscataway, NJ) at 0.8–1 mA/cm^2 for 45 min at room temperature. The blots were blocked in PBS containing 0.05% Tween 20 (PBST) and 5% nonfat dry milk, followed by incubation with the monoclonal antibody against phosphorylated ERK1/2 (pERK1/2) (Santa Cruz Biochem, Santa Cruz, CA). The blots were then washed and incubated with antimouse horseradish-peroxidase-labeled IgG. Subsequently, the blots were developed with the ECL Western Detection Reagent (Amersham) according to the manufacturer's instruction. The blots were stripped in PBST (pH 2.5–2.8) for 1 hour, were labeled with a monoclonal antibody against β-actin (Sigma), and were then developed as described above. Graphs of blots were quantified and normalized to the levels of actin by scanning densitometry (Bio-Rad 620 scanner, Richmond, CA) of graphs.

Immunocytochemical staining and analyses were used to determine the distribution of ERK1/2 in cross-sectional slices of the venous anastomosis on two animals 4 hours and 4 weeks after graft implantation. Immunocytochemistry was performed on frozen sections as follows. The tissue was embedded in OTC and frozen in Freon cooled in liquid nitrogen. Cross sections (5–8 μm thick) were cut in a cryostat at −20°C and then brought to room temperature at the time of staining. Sections were washed in PBS, quenched with 3% hydrogen peroxide for 5 min, and blocked with 10% normal goat serum in 1% BSA-PBST for 30 min. Sections were incubated with various primary antibodies at 4°C overnight. After washing with PBS, the sections were incubated with corresponding biotinylated secondary antibodies for 30 min (Envision kit). The antigen-antibody binding was detected by DAB substrate chromogen system (HK153-5K from Biogenex). The slides were washed, counterstained with hematoxylin for 60 s, dehydrated, and cover-slipped. For a negative control, the sections were incubated in PBS without the primary antibody. With a digital light microscope facility (Zeiss Axioskop microscope, Zeiss Axiocam camera with PhotoShop plug-in and Power Macintosh 9600/300 computer), each cross-section was scanned and saved for further analysis. With the aid of Adobe PhotoShop and NIH Image 1.62, semi-quantitative measurements of the density (in pixels) of the specific immunostains for ERK1/2 in the intima for each quadrant were determined; a standard density scale ranging from 210 to 255 was used for densely stained areas with ERK1/2.

Results

Experimental Measurements. Figure 6 shows velocity vectors, turbulence fluctuation amplitudes and Reynolds stresses for Re =1060. SI units are used except for the Reynolds stresses, where dynes/cm^2 follow the convention established in the hemolysis and arterial-wall-disease literature. At $X=-6.6D$, flow enters the model via the graft and DVS with a fully developed laminar (parabolic) velocity profile (Fig. 6*a*). The two streams enter the anastomosis region and merge, accelerating as they move proxi-

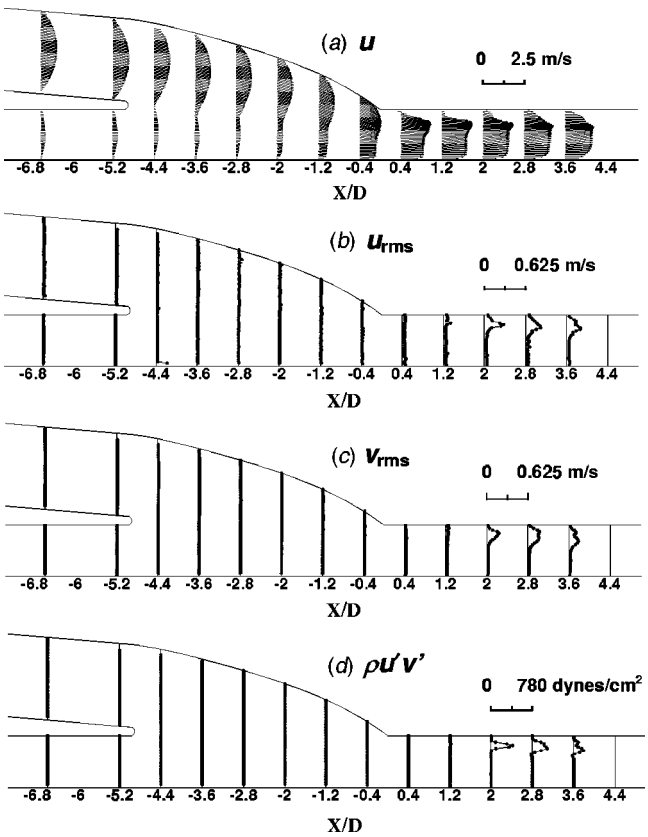

Fig. 6 LDA velocity measurements at Re=1060 in the plane of the bifurcation: (*a*) mean velocity vectors, (*b*) *u*-component turbulent fluctuations, u_{rms}, (*c*) v-component turbulent fluctuations, v_{rms}, (*d*) Reynolds stress, $\rho u' v'$

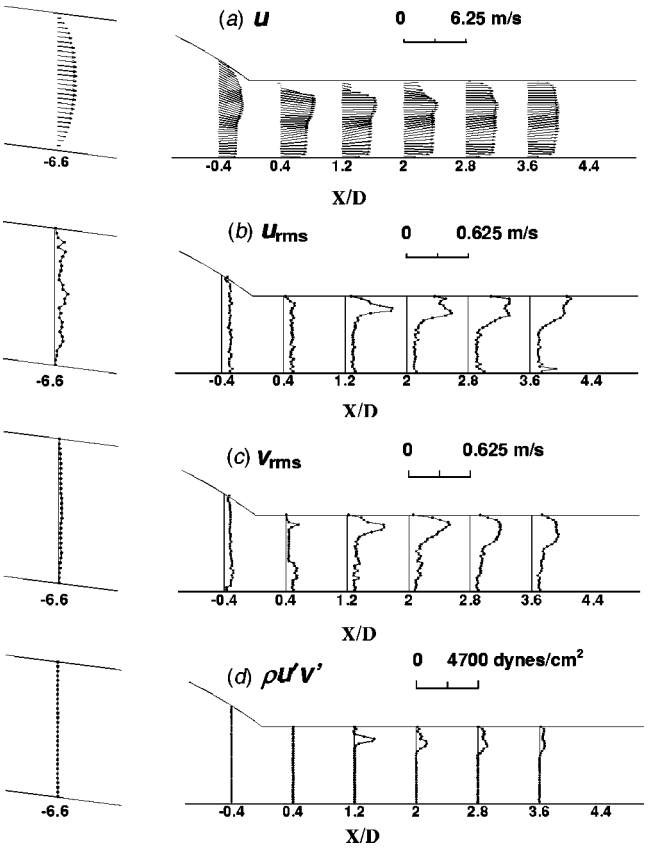

Fig. 7 LDA velocity measurements at Re=1820 in the plane of the bifurcation: (*a*) mean velocity vectors, (*b*) *u*-component turbulent fluctuations, u_{rms}, (*c*) v-component turbulent fluctuations, v_{rms}, (*d*) Reynolds stress, $\rho u' v'$

mally because of the reduction in cross-sectional area. A small separation region downstream of the toe is evidenced by a retrograde vector near the wall at $X=+0.4D$. Turbulent fluctuations and Reynolds stresses are small except near the toe side of the PVS starting at $X=+2.0D$ (Figs. 6*b*, *c*, and *d*). The maximum fluctuation amplitude (u_{rms} at $X=+2.0D$) is 0.3 m/s, which is ~25% of the local mean velocity.

The normally quoted threshold Re for transition in a pipe is at best approximate and is valid only for an extremely long and smooth straight pipe. Turbulence can be tripped at lower Reynolds numbers but cannot be sustained below about 2300. The recirculating-flow rig used here was not designed with special precautions against flow instability, since no such ideal circumstances can be assumed in biological flows. At Re=1820 (Fig. 7), we observed a small but distinct degree of blunting of the graft inlet profile, indicating the flow to be near transition. The velocity profile at the downstream (proximal) end of the anastomosis was not greatly different from that at Re=1060, but the turbulent fluctuation amplitude was considerably higher (0.47 m/s), although it was lower as a percentage (~15%) of the local mean velocity. The fluctuation amplitude was nearly constant (3–5%) across the vessel just before ($-0.4D$) and after ($+0.4D$) the entrance to the PVS. The separated eddy just downstream of the toe penetrated further into the lumen at $X=+0.4D$ than at Re=1060, but reattachment still occurred before $X=+1.2D$. This penetration distance was examined more carefully in separate experiments and was found to be ~$0.1D$ diameters measured from the hood side. Further downstream, the profiles generally resembled those found at Re=1060, except that at $X=+3.6D$ the *u*-component profile had become blunt and almost symmetrical. Turbulent fluctuations and Reynolds stresses were elevated relative to those at Re =1060 and reached significant amplitudes closer to the toe, at X

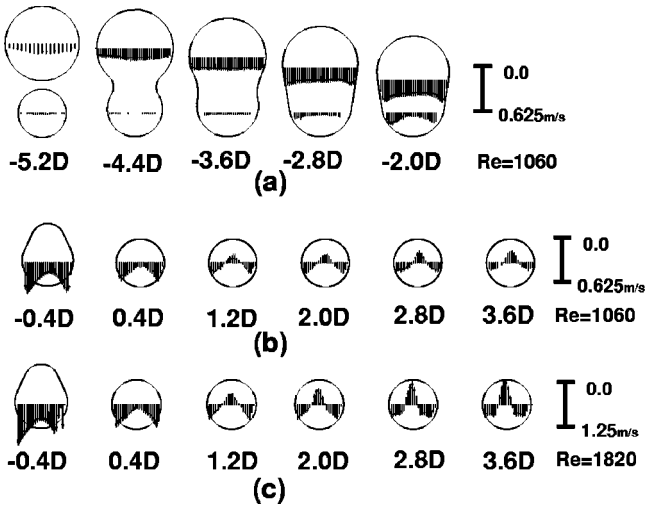

Fig. 8 LDA measurements of mean velocity for velocity component parallel to the plane of the bifurcation and perpendicular to the floor of the graft (v_{mean}) at different axial locations. (*a*) secondary flow within the anastomosis at Re=1060, (*b*) secondary flow within and just downstream of the PVS at Re =1060, and (*c*) secondary flow within and just downstream of the PVS at Re=1820. Note that these are 1-D vectors of *v*-component amplitude; the other component in the cross-section plane, the *w*-component (flow normal to the bifurcation plane), was not measured.

=+1.2*D*. The maximum Reynolds stress was 2030 dynes/cm^2, whereas the maximum at Re=1060 was 390 dynes/cm^2. At both Reynolds numbers, the primary u_{rms} peak on the toe side split into a double peak as the maximum amplitude decayed proximally in the PVS.

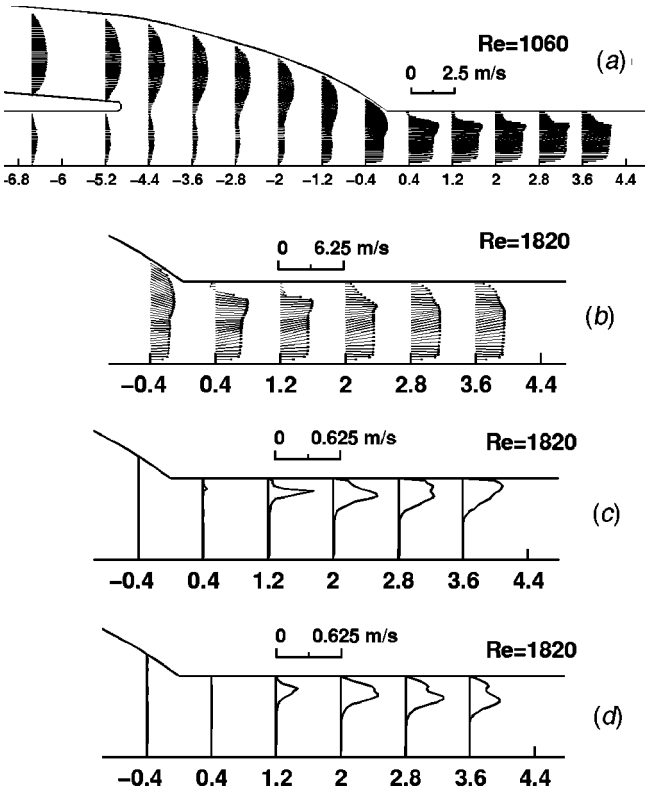

Fig. 9 CFD velocity results in the plane of the bifurcation: (*a*) mean velocity vectors at Re=1060, (*b*) mean velocity vectors at Re=1820, (*c*) *u*-component turbulent fluctuations, u_{rms}, (*d*) *v*-component turbulent fluctuations, v_{rms}

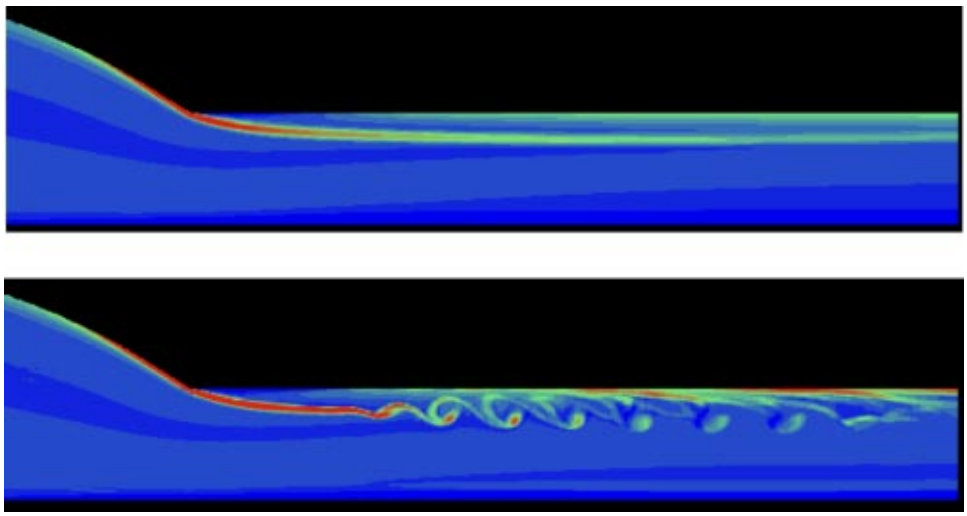

Fig. 10 CFD simulation of the instantaneous vorticity distribution at Re=1060 (top) and 1820 (bottom) in the plane of the bifurcation

The model was constructed to be symmetric about the plane of the bifurcation such that velocity profiles were expected to be symmetric about the centerline. Symmetry is evident in the profiles of velocity taken perpendicular to the midplane shown in Fig. 8. Secondary flow was more pronounced at the higher Reynolds number, as expected.

Numerical Simulations. The velocity results of the CFD simulations are shown in Fig. 9 for Reynolds numbers 1060 and 1820 in the plane of the bifurcation. Good agreement is observed between these CFD findings and the experimental results (Figs. 6 and 7) for both the profiles of velocity vectors and the fluctuation amplitudes. The general location of the separation zone agrees with the experimental results. As in the experimental results, the u_{rms} profile exhibits a sharp spike near the onset of transition, fills out, and becomes skewed toward the hood side at successive downstream stations. The double-peaked structure observed in the experimental results is also evident in the numerical ν_{rms} profiles.

At Re=1060 the flow is essentially laminar, while at Re =1820 coherent structures can be observed downstream of the separation point near the toe. This is shown in the comparison of instantaneous spanwise vorticity in the plane of the bifurcation (Fig. 10). The coherent structures are more clearly identified by using the λ_2 criterion of Jeong and Hussain [47] as shown in Fig. 11. The colors in these figures represent the instantaneous 3D-pressure distribution on the lumen surface and on the λ_2 isosurfaces.

Figure 12 shows the time-average predicted WSS within and just before the PVS portion of the venous anastomosis on the hood and floor. WSS is generally high throughout the PVS as expected because of the large flow-rate in these AV grafts. A spike in the WSS is present at the toe as a results of the cusp in the model geometry. WSS is directed upstream in the small region of flow reversal that extends roughly $0.7D$ and $0.8D$ downstream of the toe for Re=1060 and 1820, respectively. The distribution of WSS magnitude in the axial and circumferential directions is shown in Fig. 12*c*, where the angle θ is measured from the floor of the graft as indicated. As shown in Fig. 13, the instantaneous WSS vectors acting on the lumen surface at Re=1820 are of a complex pattern and not all directed axially. These WSS patterns are translated downstream as the generating coherent structures are advected with the flow.

Vibration Measurements. Passive measurements of *in vivo* vein surface motion (radial vibration velocity) were made with LDV at regions A, B, and C (Fig. 5). The smallest and largest levels of vein vibration were detected at positions A and B respectively, as seen in Fig. 14. Regional variation in turbulence-induced vibration intensity was evaluated by computing the root mean squared (RMS) value of the vibration velocity in the frequency

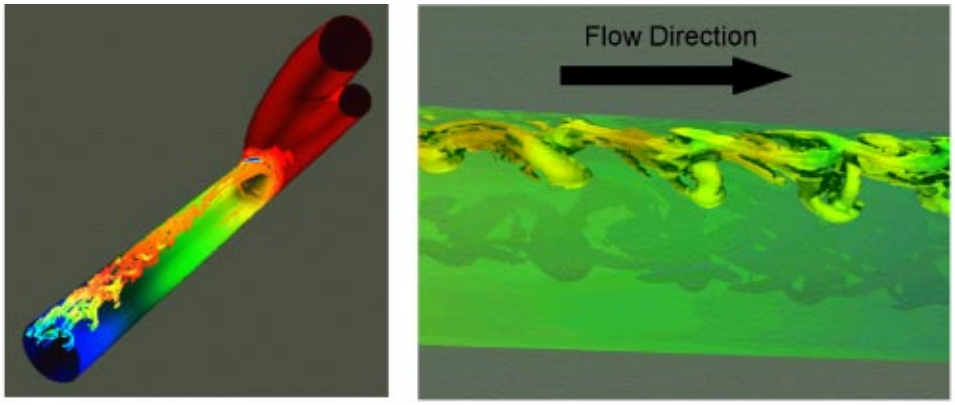

Fig. 11 Coherent structures (vortices) identified using the λ_2 criterion of Jong and Hussain [47]. Color represents the instantaneous 3D-pressure distribution. Left-full view, Right-detailed view downstream of toe.

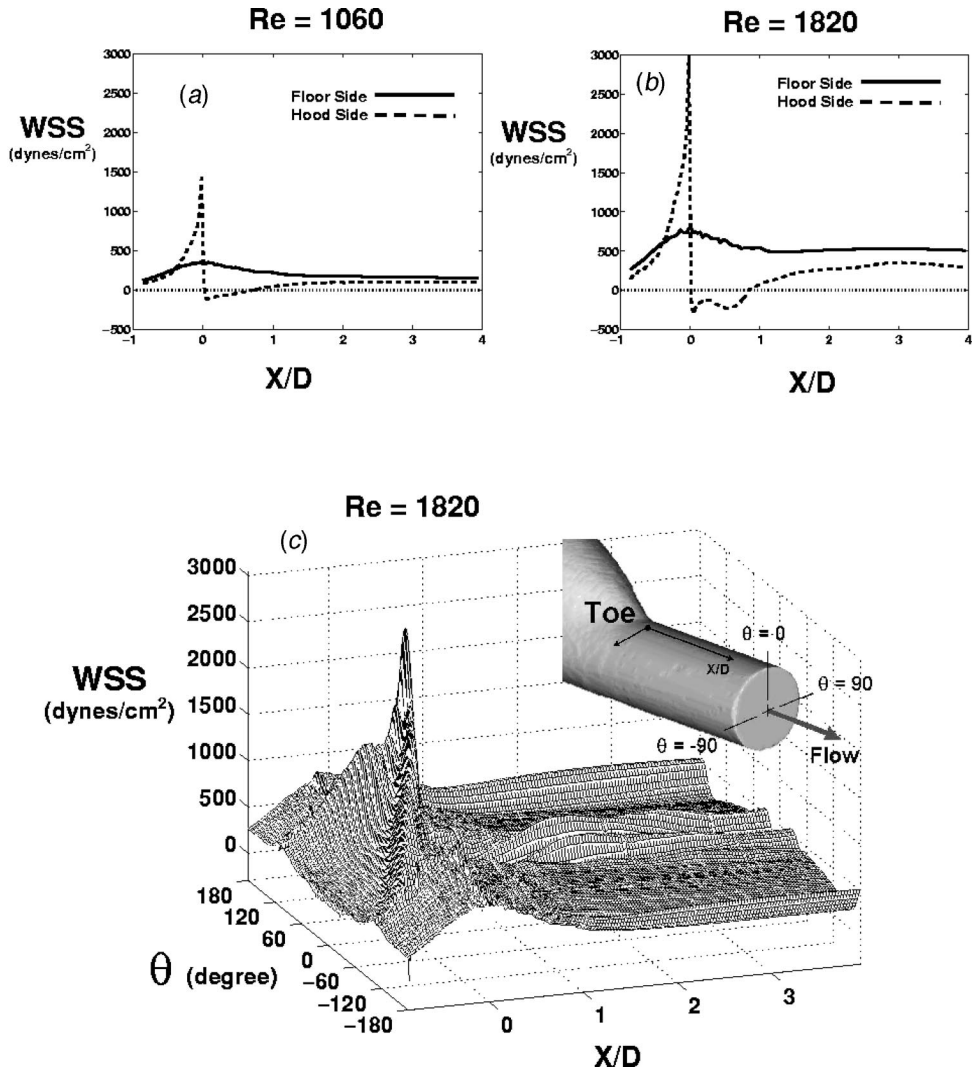

Fig. 12 Time average WSS computed from CFD simulations (*a*) axial distribution (θ=0°) at Re=1060, (*b*) axial distribution (θ=0°) at Re=1820, (*c*) axial and circumferential distribution at Re=1820. (Note: the spike in WSS at the toe of the graft is caused by the sharp angle of the flow model.)

range 40–800 Hz. The low-frequency range (<40 Hz) was excluded by frequency-domain truncation because vein-wall vibration in this frequency range is not related to turbulent fluctuations of velocity and pressure. The turbulence intensity was two- and five-fold greater at position B when compared with positions C

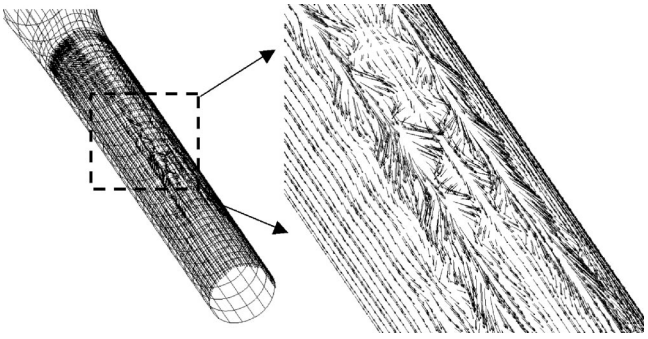

Fig. 13 Instantaneous view from the CFD results of the WSS vectors on the lumen surface (LEFT), zoom view in which the complex pattern of WSS magnitude and direction is evident (RIGHT)

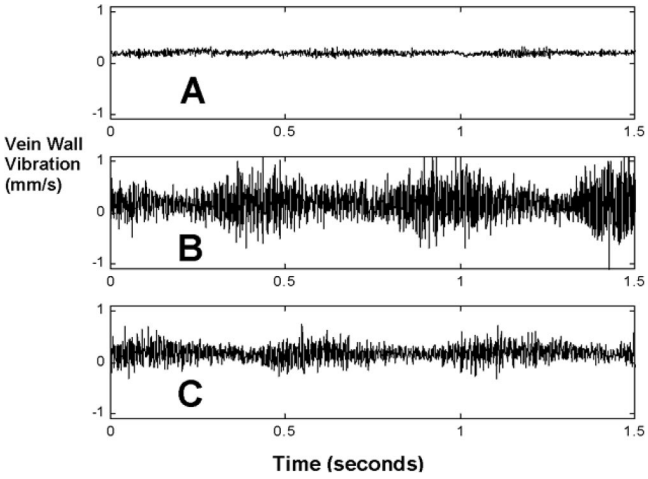

Fig. 14 Vein-wall vibration velocity measured directly on the vein during surgery. Note the greater vibration at region B compared to regions A and C. Regions of anastomosis are shown in Fig. 5.

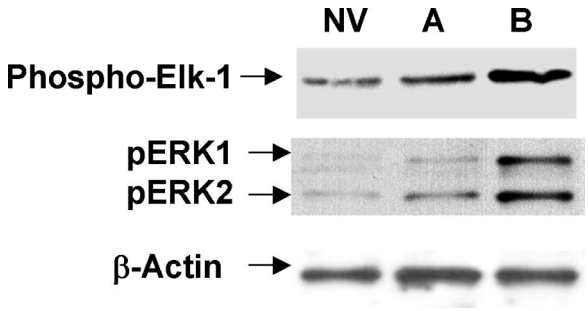

Fig. 15 MAP kinase assay (top panel) and Western blot assay (center and bottom panels) for ERK1/2 activity and phosphorylation from different regions (A and B) of anastomotic vein and normal control vein (NV). The bands of *β*-Actin indicate the loading conditions.

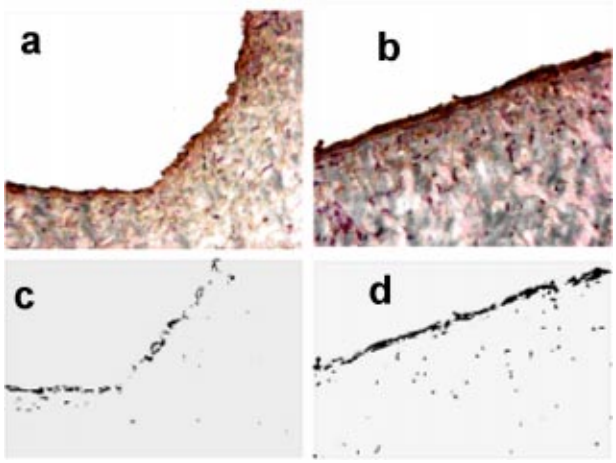

Fig. 17 Immunolocalization of ERK1/2 at four weeks in (*a*) region of reduced vein wall vibration (region A) and (*b*) region of elevated vein-wall vibration (region B). Densitometric analysis of immunostaining intensity for (*a*) and (*b*) is shown in (*c*) and (*d*). ERK1/2 immunostaining is predominately localized in the intimal region and is 2.5 fold greater in (*b*) compared to (*a*). Magnification 40X.

and A, respectively. In a related study examining multiple AV grafts (48), not all measurements showed this distribution of vibration intensity. However, the overall trend in vibration intensity was consistent with this sample measurement.

Molecular Biology. pERK1/2 and its activity (Elk1 phosphorylation) were measured at the different regions of the anastomotic vein segment with high (region B) and low (region A) vibration intensity levels, 4 hours after creation of the anastomosis. The ERK1/2 activity was determined by phosphorylation of the immediate downstream transcription factor Elk-1 that is known to be involved in growth and differentiation. Using densitometric analysis, we found a three-fold increase in pERK1/2 at this early time point at region B when compared to region A (Fig. 15 center panel). This was associated with a corresponding increase in the phosphorylation of the Elk1, implicating enhanced vein-wall vibration in the rapid activation of the putative mechanotransduction pathways (Fig. 15, top panel). The bands of *β*-Actin indicate that the loading conditions were similar for each case (Fig. 15, bottom panel).

At 4 hours ERK1/2 localized predominantly at regions of elevated vibration intensity (region B) within the intimal and medial VSMCs. Densitometric analysis revealed at least a three-fold increase in ERK1/2 immunostaining at region B when compared to normal control vein and regions exposed to reduced vibration intensity (region A) as shown in Figs. 16*a*, *b* and *c*. This pattern of localization persisted at 4 weeks. Densely stained regions occupied close to 37% of the intimal/medial area at regions of elevated vibration intensity compared to 10–15% in regions of reduced vibration intensity and normal vein. Additionally the intima/media thickness was greater (more than 2 fold) at region B when compared with region A (Figs. 17*a* and *b*).

We conducted cellular immunolocalization studies in contiguous cross-sections, 5 μm apart, located approximately 4–5 mm from the suture line in regions of reduced and elevated vein wall vibration (regions A and B, respectively). The sections were investigated at 4 hours and 4 weeks. At 4 hours there was minimal T cell (anti-CD4 antibody) and macrophage (anti-CD11b/-Mac1 antibody) infiltration across the anastomotic regions. ERK1/2 immunostaining was increased, however, in region B within endothelial (anti-CD31 antibody) and medial VSMC (anti-actin antibody), as shown in Fig. 16. At 4 weeks, a modest increase in T lymphocyte and macrophage infiltration was observed across the anastomotic regions. This is illustrated in Fig. 18, where the ERK1/2 immunostaining is noted in the intima (Fig. 18*a*) with no evidence of colocalization of T-lymphocytes (Fig. 18*b*) and macrophage infiltration (Fig. 18*c*) in immediately adjacent cross-sections (5 μ apart).

Discussion

The results presented describe many of the key features of the flow field to be expected within the venous anastomosis of a di-

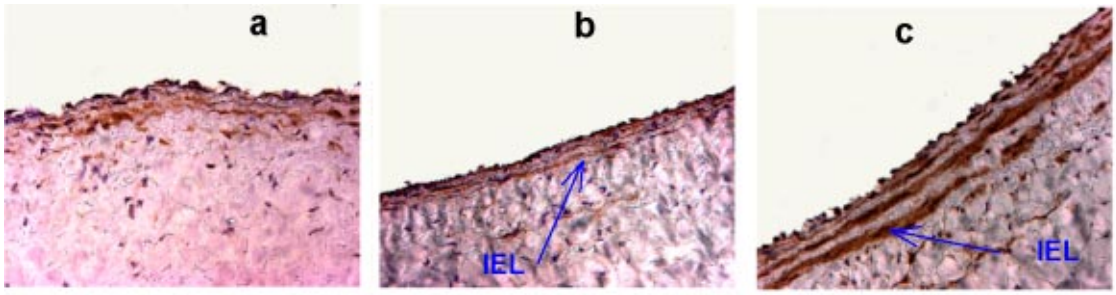

Fig. 16 Immunolocalization of ERK1/2 at four hours in (*a*) normal vein, (*b*) region of reduced vein wall vibration (region A), (*c*) and region of elevated vein wall vibration (region B). ERK1/2 immunostaining is represented by dark brown color in the intima and media. Note the markedly increased ERK1/2 density in the intimal and media of vein wall with elevated vibration (*c*) relative to (*a*) and (*b*). Internal elastic lamina is indicated as IEL (40X magnification).

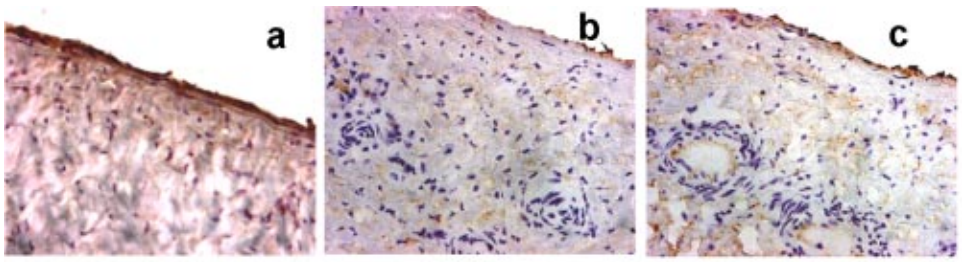

Fig. 18 Immunostaining for (*a*) ERK1/2, (*b*) T-lymphocytes and (*c*) macrophages in region of elevated vein wall vibration (region B) at 4 weeks in immediately adjacent cross sections (5 μ apart). Note the lack of co-localization between ERK1/2 and the inflammatory cells.

alysis patient's blood-access AV graft. The experimental and numerical models have examined Reynolds numbers representing peak and mean values of the physiological range indicated by *in vivo* measurements. At these Reynolds numbers, the flow is highly unsteady, complex, and three dimensional, with transition to turbulence as a prominent feature. *In vivo* measurements on the porcine AV graft model identify regions of high vein-wall vibration downstream of the toe in the PVS, where significant velocity fluctuations are indicated by the experimental and numerical models. This high vein-wall vibration region was associated with elevated activity levels of ERK1/2 and intimal thickening. This work gives preliminary evidence of a possible relationship between vein-wall vibration and the ERK1/2 mechanotransduction pathway. However, more detailed studies are required to understand the independent role of WSS and vein-wall vibration on VAIH at the venous anastomosis of an AV graft.

In normal arterial flows, pulsatility plays an important role, and a quasi-steady inflow assumption may not apply. AV graft flows are abnormal in this respect, in that the elevated mean flow-rate gives rise to a reduced pulsatility index. The results under steady inflow conditions are therefore useful for several reasons. First, a low pulsatility index implies that the unsteadiness is of reduced importance. Second, steady inflow provides insight into the causes of specific flow features, which may also exist in pulsatile flow, and allows them to be specifically identified as geometric phenomena rather than unsteady phenomena. Third, numerical solutions of the Navier-Stokes equations require experimental measurements for code validation. Such measurements are particularly needed for transitional flows. These results provide data for code validation of the 3D steady-flow solution inside a mathematically defined, but clinically realistic, venous anastomotic geometry.

Both the experimental and computational models were rigid. We expect the rigid-model assumption to be reasonable because both vein and PTFE have small compliance at these pressures and because the pressure variation in the AV graft is much lower than that in arteries. The mean and variation in pressure measured in our animal study were $\sim$20 and $\pm$1 mmHg, respectively, versus $\sim$100 and $\pm$20 mmHg for arteries. While the compliance of the porcine vein at 20 mmHg has not been reported in the literature, Brossollet [49] measured the compliance of a healthy canine saphenous vein to be 0.13%/mmHg at 21 mmHg and *in vivo* length. Brossollet also reported compliance results based on a polynomial fit method he developed. The mean and standard deviation of compliance for 19 specimens were 0.28 and 0.11%/mmHg, respectively, using this method. Thus, vein-wall motion associated with the cardiac cycle is significantly lower ($<$1.0% of the diameter) than that typically found in arteries. In addition, the high frequency pressure fluctuations did not create significant vein-wall displacement. The high-frequency vein-wall motion was quantified by integration of the *in vivo* vein-wall velocity data (Fig. 14) after band-pass filtering (40–800 Hz) to remove effects of vein translation. The amplitude of vein-wall displacement in this frequency range was small (<1 μm, or 0.025% of the diameter).

Both the experimental and computational models were symmetric about the bifurcation plane. Symmetry is not physiological. Sherwin et al. [18] examined the influence of out-of-plane geometry on flow within the end-to-side anastomosis. They found that nonplanar flow notably alters the distribution of velocity and WSS. This observation underscores the importance of subject-specific geometry in the study of graft hemodynamics. The present results provide insight into the features of transitional flow in a symmetric AV graft geometry that may also be present in nonplanar flows. Future studies in nonplanar geometries at these Reynolds numbers may identify new features that are specific to nonplanar flow.

The distinguishing feature in the AV graft is its transitional nature. However, strong secondary flow patterns were also present and found to be opposite to those normally reported for anastomotic geometries. Previous research on arterial distal end-to-side anastomoses reported a classic Dean flow pattern in the distal outlet segment (DOS) [12,16], which is referred to as the PVS here. In particular, Ojha et al. [16] found the velocity profiles in a different geometry to be skewed toward the floor at Reynolds numbers 250–1300. The turning of the flow as it enters the DOS sets up a Dean flow pattern in which flow on the lateral walls moves upward (toward the hood). This same pattern was observed by Loth et al. [12] with the geometry of the present study and low Reynolds number (Re=140). In addition, each of these studies differed from the present study in DVS flow direction and magnitude.

In the present study, the PVS secondary-flow pattern shown in Fig. 8 is set up when the graft inlet flow impinges on the anastomosis hood and is deflected downward. This downward stream curvature causes a Dean's flow opposite to that observed in [12,16]. This pattern persists when the graft inlet flow enters the PVS and merges with the weaker stream arriving from the DVS. Once the two streams merge in the PVS, the flow is undeveloped and consequently has a reduced tendency to form a Dean flow pattern as flow from the graft turns to align with the horizontal vein axis. As can be seen in Figs. 6*a*, 7*a*, 9*a*, and 9*b*, the axial profile in the PVS is skewed toward the toe side, again, opposite to that reported in [12,16]. The PVS secondary flow pattern is qualitatively similar at both Reynolds numbers examined but is strongest at Re=1820.

The coherent structures observed in Fig. 11 are similar to the chains of hairpin vortices associated with transitional and turbulent boundary layers [50,51]. The hairpin exhibits bilateral symmetry about the bifurcation plane, with a central head that lifts down (away) from the toe-side and that is connected to a pair of counter-rotating vortices that form the legs of the hairpin. The rotation of the legs is such that it sweeps near-wall fluid in toward the symmetry plane. As described in [49,50], the tails of each hairpin vortex intertwine with the tails of the hairpin immediately upstream.

An important feature of the AV-graft hemodynamic environment is the high frequency of the WSS and pressure fluctuations. Velocity-time traces from the numerical simulation at Re=1820

indicate a fundamental frequency of 715 Hz in the PVS downstream of the toe ($X/D=+0.4$, region B) associated with the passage of coherent structures. Peak power values of vein-wall vibration during the *in vivo* study were ~300 Hz as taken from a power spectrum of time trace B shown in Fig. 14. The velocity-time traces from the LDA experimental provide RMS and Reynolds stress values. However, the data rate was insufficient to provide quantitative information about the spectral content of the velocity fluctuations. The fact that the numerical frequency is larger than that measured *in vivo* is probably attributable to the variations in geometry and different Reynolds number *in vivo* (typical mean Re_{vivo}~1100–1500). While the Strouhal number (non-dimensional frequency) should be the same for a fixed geometry and Reynolds number, the dimensional frequency will be proportional to V/D. The increase in vein-wall vibration downstream of the toe is in agreement with numerical and experimental results. However, vein-wall vibration was larger in region B while the numerical and experimental results indicate velocity fluctuations to be the same in regions B and C or even higher in region C. In addition to differences in geometry and Reynolds number, the transfer of vibration energy from velocity fluctuations to the vein wall may alter the vein-wall vibration distribution and modulate the frequency.

Immunocytochemical qualitative and semi-quantitative analysis of ERK1/2 co-localization with T-lymphocytes, macrophages, endothelial cells and VSMCs at the suture-line region and at regions of the venous anastomosis were performed on regions where varied levels of vein-wall vibration prevail proximal and distal to the suture-line junction. Such studies were conducted at 4 hours and 4 weeks after porcine AV graft implantation. These studies indicated (1) ERK1/2 co-localizes predominately in the intima (endothelial cells) and to a lesser degree in the medial VSMCs, (2) ERK1/2 immunostaining is greatly enhanced in regions of elevated vein-wall vibration when compared with regions of suture-line injury or reduced vein-wall vibration, and (3) ERK1/2 immunostaining appears unrelated to T-lymphocyte and macrophage infiltration. This is most evident at the suture region where significant mural injury and inflammation are present yet ERK1/2 immunostaining is less striking than at regions of elevated vein-wall vibration. These findings indicate that biomechanical variables, namely, turbulence-induced vein-wall vibrations may play an important role in regulating MAPK activation in the intimal endothelial cells of the venous wall. The contribution of inflammation to ERK1/2 activation appears minimal in this experimental model.

One question that arises from this research concerns the relative importance of WSS and turbulence in the development of VAIH and eventual failure of AV grafts. The localization of IH has long been thought to be correlated with low and oscillating WSS. In a canine animal study of IH in arterial grafts, Keynton et al. [52] found IH to be correlated with mean and oscillatory shear index. In another study, Loth et al. [13] have shown that, while a correlation is seen between IH and the reciprocal of WSS, the degree of correlation is reduced by the influence of material and injury. In the present study of the AV graft, WSS is nearly one order of magnitude greater than that found in the arterial distal anastomosis. Still, in the AV graft, a region of flow separation is present that is nearly one vein diameter in length and is associated with low WSS near the reattachment point. Another difference is that the fluctuating WSS (see Fig. 13) at these transitional Reynolds numbers is different both in magnitude and direction from that in arterial grafts. The preliminary biological studies give evidence that the tissue proximal (downstream) of the toe within the PVS has begun to elicit the complex cascade of intracellular signaling events that typically occur in response to WSS stimulation of endothelial cells and VSMCs. This is shown by the increases in activity of ERK1/2 after 4 hours and 4 weeks.

This complex WSS pattern is accompanied by a distribution of vein-wall vibration. High-vibration regions are located just downstream of the toe in the PVS that coincide with the regions of greater WSS fluctuation. Further downstream, vein-wall vibration and velocity fluctuations decrease. Since the region of large vein-wall vibration is near the region of the flow separation, it is difficult to separate their effects. This is a limitation of the presented results. Further research must be conducted in which the detailed circumferential distribution of ERK1/2 is examined, since the low-WSS region is confined to the toe-side of the PVS while vein-wall vibration appears to be more diffuse, encompassing the toe side, side walls, and floor side of the PVS. However, based on the results from Fillinger et al. on the correlation between tissue vibration and VAIH in a canine study [4] and present preliminary results, we suspect that vibration plays a more dominant role than WSS within the AV graft. Fillinger et al. also found VAIH to be correlated with Reynolds number. It seems unlikely that grafts with greater Reynolds numbers would also be associated with larger regions of low and oscillating WSS. Nonetheless, in the future we plan to investigate both vein-wall vibration and WSS within experimental AV grafts in further detail, with the aim of separating these two effects.

Conclusions

We have presented evidence that the flow field within the venous anastomosis of an AV graft is transitional for cases in which the Reynolds number is under 2000. First, this was demonstrated by spectral broadening of the velocity measurement on a human by Doppler ultrasound. Second, large values of velocity fluctuations were measured within a model *in vitro* that closely represents the *in vivo* geometry under steady-flow conditions that match the mean-flow conditions observed *in vivo*. Third, numerical simulations on the same geometry for steady-flow conditions revealed the detailed pattern of coherent structures within the PVS and demonstrated the large WSS values present at these Reynolds numbers. Fourth, *in vivo* LDV measurements showed vein-wall vibration with dominant frequencies that are high (~300 Hz) and consistent with those observed in the experimental and numerical models. Additionally, we have presented preliminary results that implicate vein-wall vibration as a possible biomechanical stimulus for the activation of ERK1/2 in the vein wall. Future work is needed to determine the precise relationship between AV graft failure and fluid-dynamic variables such as velocity fluctuations and WSS, as well as their relative importance.

Acknowledgments

Many thanks to Dawn Hodge for her help in acquiring the CT images of the AV graft model, Steven Jones for insightful discussion, Henry Tufo, for assistance with the simulations, and Wojciech Kalata for help on the image processing. This work was supported by the Mathematical, Information, the Whitaker Foundation (RG-01-0198), and Computational Sciences Division subprogram of the Office of Advanced Scientific Computing Research, U.S. Department of Energy, under Contract W-31-109-Eng-38. We also thank the Faculty Research Participation program, administered by DEP, at Argonne National Laboratory, which was instrumental in enabling the collaboration that resulted in this study. This work was also supported in part by W. L. Gore and Associates.

References

[1] Kanterman, R. Y., Vesely, T. M., Pilgram, T. K., Guy, B. W., Windus, D. W., and Picus, D., 1995, "Dialysis Access Grafts: Anatomic Location of Venous Stenosis and Results of Angioplasty," Radiology, **195**, pp. 135–9.

[2] Fillinger, M. F., Kerns, D. B., Bruch, D., Reinitz, E. R., and Schwartz, R. A., 1990, "Does the End-to-end Venous Anastomosis Offer a Functional Advantage Over the End-to-side Venous Anastomosis in High-output Arteriovenous Grafts?," J. Vasc. Surg., **12**, pp. 676–88; discussion 688–90.

[3] Fillinger, M. F., Kerns, D. B., and Schwartz, R. A., 1991, "Hemodynamics and Intimal Hyperplasia," Vascular Access for Hemodialysis-II, B. G. Sommer and M. L. Henry, eds., W. L. Gore & Associates, Inc., and Precept Press, Inc., pp. 21–51.

[4] Fillinger, M. F., Reinitz, E. R., Schwartz, R. A., Resetarits, D. E., Paskanik, A. M., Bruch, D., and Bredenberg, C. E., 1990, ''Graft Geometry and Venous Intimal-medial Hyperplasia in Arteriovenous Loop Grafts,'' J. Vasc. Surg., **11**, pp. 556–66.
[5] Fillinger, M. F., and Schwartz, R. A., 1993, ''Volumetric Blood Flow Measurement With Color Doppler Ultrasonography: The Importance of Visual Clues,'' J. Ultrasound Med., **12**, pp. 123–30.
[6] Ethier, C. R., Prakash, S., Steinman, D. A., Leask, R. L., Couch, G. C., and Ojha, M., 2000, ''Steady Flow Separation Patterns in a 45 Degree Junction,'' J. Fluid Mech., **411**, pp. 1–38.
[7] Ethier, C. R., Steinman, D. A., Zhang, X., Karpik, S. R., and Ojha, M., 1998, ''Flow Waveform Effects on End-to-side Anastomotic Flow Patterns,'' J. Biomech., **31**, pp. 609–17.
[8] Jones, S. A., Giddens, D. P., Loth, F., Zarins, C. K., Kajiya, F., Morita, I., Hiramatsu, O., Ogasawara, Y., and Tsujioka, K., 1997, ''In-vivo Measurements of Blood Flow Velocity Profiles in Canine Ilio-Femoral Anastomotic Bypass Grafts,'' J. Biomech. Eng., **119**, pp. 30–8.
[9] Keynton, R. S., Evancho, M. M., Sims, R. L., and Rittgers, S. E., 1999, ''The Effect of Graft Caliber Upon Wall Shear Within *In Vivo* Distal Vascular Anastomoses,'' J. Biomech. Eng., **121**, pp. 79–88.
[10] Keynton, R. S., Rittgers, S. E., and Shu, M. C., 1991, ''The Effect of Angle and Flow Rate Upon Hemodynamics in Distal Vascular Graft Anastomoses: An *In Vitro* Model Study,'' J. Biomech. Eng., **113**, pp. 458–63.
[11] Lei, M., Giddens, D. P., Jones, S. A., Loth, F., and Bassiouny, H., 2001, ''Pulsatile Flow in an End-to-side Vascular Graft Model: Comparison of Computations With Experimental Data,'' J. Biomech. Eng., **123**, pp. 80–7.
[12] Loth, F., Jones, S. A., Giddens, D. P., Bassiouny, H. S., Glagov, S., and Zarins, C. K., 1997, ''Measurements of Velocity and Wall Shear Stress Inside a PTFE Vascular Graft Model Under Steady Flow Conditions,'' J. Biomech. Eng., **119**, pp. 187–94.
[13] Loth, F., Jones, S. A., Zarins, C. K., Giddens, D. P., Nassar, R. F., Glagov, S., and Bassiouny, H., 2001, ''Relative Contribution of Wall Shear Stress and Injury in Experimental Intimal Thickening at PTFE End-to-side Arterial Anastomoses,'' J. Biomech. Eng., **124**, pp. 44–51.
[14] Ojha, M., 1993, ''Spatial and Temporal Variations of Wall Shear Stress Within an End-to-side Arterial Anastomosis Model,'' J. Biomech., **26**, pp. 1377–88.
[15] Ojha, M., 1994, ''Wall Shear Stress Temporal Gradient and Anastomotic Intimal Hyperplasia,'' Circ. Res., **74**, pp. 1227–31.
[16] Ojha, M., Ethier, C. R., Johnston, K. W., and Cobbold, R. S., 1990, ''Steady and Pulsatile Flow Fields in an End-to-side Arterial Anastomosis Model,'' J. Vasc. Surg., **12**, pp. 747–53.
[17] Ojha, M., Leask, R. L., Johnston, K. W., David, T. E., and Butany, J., 2000, ''Histology and Morphology of 59 Internal Thoracic Artery Grafts and Their Distal Anastomoses,'' Ann. Thorac. Surg. , **70**, pp. 1338–44.
[18] Sherwin, S. J., Shah, O., Doorly, D. J., Peiro, J., Papaharilaou, Y., Watkins, N., Caro, C. G., and Dumoulin, C. L., 2000, ''The Influence of Out-of-plane Geometry on the Flow Within a Distal End-to-side Anastomosis,'' J. Biomech. Eng., **122**, pp. 86–95.
[19] White, S. S., Zarins, C. K., Giddens, D. P., Bassiouny, H., Loth, F., Jones, S. A., and Glagov, S., 1993, ''Hemodynamic Patterns in Two Models of End-to-side Vascular Graft Anastomoses: Effects of Pulsatility, Flow Division, Reynolds Number, and Hood Length,'' J. Biomech. Eng., **115**, pp. 104–11.
[20] Glagov, S., Giddens, D. P., Bassiouny, H., White, S. S., and Zarins, C. K., 1991, ''Hemodynamic Effects and Tissue Reactions at Graft to Vein Anastomosis for Vascular Access,'' Vascular Access for Hemodialysis-II, B. G. Sommer and M. L. Henry, eds., W. L. Gore & Associates, Inc., and Precept Press, Inc., pp. 3–20.
[21] Shu, M. C., and Hwang, N. H., 1988, ''Flow Phenomena in Compliant and Noncompliant Arteriovenous Grafts,'' ASAIO Trans., **34**, pp. 519–23.
[22] Shu, M. C., and Hwang, N. H., 1991, ''Haemodynamics of Angioaccess Venous Anastomoses,'' J. Biomed. Eng., **13**, pp. 103–12.
[23] Shu, M. C., Noon, G. P., and Hwang, N. H., 1987, ''Phasic Flow Patterns at a Hemodialysis Venous Anastomosis,'' Biorheology, **24**, pp. 711–22.
[24] Shu, M. C., Noon, G. P., and Hwang, N. H., 1987, ''Flow Profiles and Wall Shear Stress Distribution at a Hemodialysis Venous Anastomosis: Preliminary Study,'' Biorheology, **24**, pp. 723–35.
[25] Ene-Iordache, B., Mosconi, L., Remuzzi, G., and Remuzzi, A., 2001, ''Computational Fluid Dynamics of a Vascular Access Case for Hemodialysis,'' J. Biomech. Eng., **123**, pp. 284–92.
[26] Nagel, T., Resnick, N., Forbes, D., and Gimbrone, M. A. J., 1999, ''Vascular Endothelial Cells Respond to Spatial Gradients in Fluid Shear Stress by Enhanced Activation of Transcription Factors,'' Arterioscler., Thromb., Vasc. Biol., **19**, pp. 1825–1834.
[27] Bao, X., Lu, C., and Frangos, J. A., 1999, ''Temporal Gradient in Shear but not Steady Shear Stress Induced PDGF-A and MCP-1 Expression in Endothelial Cells: Role of NO, NFkB, and egr-1,'' Arterioscler., Thromb., Vasc. Biol., **19**, pp. 996–1003.
[28] Yan, C., Takahashi, M., Okuda, M., Lee, J. D., and Berk, B. C., 1999, ''Fluid Shear Stress Stimulates Big Mitogen-activated Protein Kinase 1 (BMK1) Activity in Endothelial Cells: Dependence on Tyrosine Kinases and Intracellular Calcium,'' J. Biol. Chem., **274**, pp. 143–50.
[29] Glagov, S., 1994, ''Intimal Hyperplasia, Vascular Modeling, and the Restenosis Problem,'' Circulation, **89**, pp. 2888–91.
[30] Zou, Y., Hu, Y., Metzler, B., and Xu, Q., 1998, ''Signal Transduction in Arteriosclerosis: Mechanical Stress-activated MAP Kinases in Vascular Smooth Muscle Cells (review),'' Int. J. Mol. Med., **1**, pp. 827–34.
[31] Traub, O., and Berk, B. C., 1998, ''Laminar Shear Stress: Mechanisms by Which Endothelial Cells Transduce an Atheroprotective Force,'' Arterioscler., Thromb., Vasc. Biol., **18**, pp. 677–85.
[32] Bassiouny, H. S., Song, R. H., Hong, X. F., Singh, A., Kocharyan, H., and Glagov, S., 1998, ''Flow Regulation of 72-kD Collagenase IV (MMP-2) After Experimental Arterial Injury,'' Circulation, **98**, pp. 157–63.
[33] Tseng, H., Peterson, T. E., and Berk, B. C., 1995, ''Fluid Shear Stress Stimulates Mitogen-Activated Protein Kinase in Endothelial Cells,'' Circ. Res., **77**, pp. 869–78.
[34] Brunet, A., Roux, D., Lenormand, P., Dowd, S., Keyse, S., and Pouyssegur, J., 1999, ''Nuclear Translocation of p42/p44 Mitogen-activated Protein Kinase is Required for Growth Factor-induced Gene Expression and Cell Cycle Entry,'' EMBO J., **18**, pp. 664–74.
[35] Lenormand, P., Brondello, J. M., Brunet, A., and Pouyssegur, J., 1998, ''Growth Factor-induced p42/p44 MAPK Nuclear Translocation and Retention Requires both MAPK Activation and Neosynthesis of Nuclear Anchoring Proteins,'' J. Cell Biol., **142**, pp. 625–33.
[36] Schwachtgen, J. L., Houston, P., Campbell, C., Sukhatme, V., and Braddock, M., 1998, ''Fluid Shear Stress Activation of egr-1 Transcription in Cultured Human Endothelial and Epithelial Cells is Mediated via the Extracellular Signal-related Kinase 1/2 Mitogen-activated Protein Kinase Pathway,'' J. Clin. Invest., **101**, pp. 2540–9.
[37] Bassiouny, H. S., 1997, ''Egr-1 is Upregulated by Reduced Flow in the Injured Rabbit Carotid Artery,'' pp. I–548.
[38] Song, R. H., Kocharyan, H. K., Fortunato, J. E., Glagov, S., and Bassiouny, H. S., 2000, ''Increased Flow and Shear Stress Enhance *In Vivo* Transforming Growth Factor-betal After Experimental Arterial Injury,'' Arterioscler., Thromb., Vasc. Biol., **20**, pp. 923–30.
[39] Lindsay, R. M., Blake, P. G., Malek, P., Posen, G., Martin, B., and Bradfield, E., 1997, ''Hemodialysis Access Blood Flow Rates can be Measured by a Differential Conductivity Technique and are Predictive of Access Clotting,'' Am. J. Kidney Dis., **30**, pp. 475–82.
[40] Yedavalli, R. V., Loth, F., Yardimci, M. A., Prichard, W. F., Oshinski, J. N., Sadler, F., Charbel, F. T., and Alperin, N., 2001, ''Construction of a Physical Model of the Human Carotid Artery Based Upon *In Vivo* Magnetic Resonance Images,'' J. Biomech., **in press**, pp.
[41] Lee, S. H., Piersol, N. E., Loth, F., Fischer, P. F., Leaf, G., Smith, B., Yedavalli, R. V., Yardimci, M. A., Alperin, N., and Schwartz, L. B., 2000, ''Automated Mesh Generation of an Arterial Bifurcation Based Upon *In Vivo* MR Images,'' World Congress on Medical Physics and Bioengineering, Chicago, IL, pp. MO-G326.
[42] Fischer, P. F., and Mullen, J. S., 2001, ''Filter-based Stabilization of Spectral Element Methods,'' *Comptes Rendus de l'Académie des sciences Paris, Série I-Analyse numérique*, **332**, pp. 265–270.
[43] Fischer, P. F., 1997, ''An Overlapping Schwarz Method for Spectral Element Solution of the Incompressible Navier-Stokes Equations,'' J. Comput. Phys., **133**, pp. 84–101.
[44] Fischer, P. F., Miller, N. I., and Tufo, H. M., 2000, ''An Overlapping Schwarz Method for Spectral Element Simulation of Three-dimensional Incompressible Flows,'' *Parallel Solution of Partial Differential Equations*, P. Bjørstad and M. Luskin, eds., Springer-Verlag, Heidelberg, pp. 159–181.
[45] Royston, T. J., Mansy, H. A., and Sandler, R. H., 1999, ''Excitation and Propagation of Surface Waves on a Viscoelastic Half-space with Application to Medical Diagnosis,'' J. Acoust. Soc. Am., **106**, pp. 3678–86.
[46] Zhang, X., Royston, T. J., Mansy, H. A., and Sandler, R. H., 2001, ''Radiation Impedance of a Finite Circular Piston on a Viscoelastic Half-space with Application to Medical Diagnosis,'' J. Acoust. Soc. Am., **109**, pp. 795–802.
[47] Jeong, J., and Hussain, F., 1995, ''On the Identification of a Vortex,'' J. Fluid Mech., **285**, pp. 69–94.
[48] Lee, S. W., Loth, F., Royston, T. J., Fischer, P. F., Shaalan, W. E., and Bassiouny, H. S., ''Turbulence induced vein-wall vibration may play a role in arteriovenous dialysis graft failure,'' Proceedings of the 4th World Congress of Biomechanics, Calgary, Canada, Aug. 2002.
[49] Brossollet, L. J., 1992, ''Effects of Cryopreservation on the Biaxial Mechanical Properties of Canine Saphenous Veins,'' Ph.D. Dissertation, Department of Mechanical Engineering, Georgia Institute of Technology, Atlanta, GA.
[50] Tufo, H. M., Fischer, P. F., Papka, M. E., and Blom, K., 1999, ''Numerical Simulation and Immersive Visualization of Hairpin Vortices,'' ACM/IEEE SC99 Conf. on High Performance Networking and Computing, pp. Argonne preprint ANL/MCS P779-0899.
[51] Acalar, M. S., and Smith, C. R., 1987, ''A Study of Hairpin Vortices in a Laminar Boundary Layer. Part 1 Hairpin Vortices Generated by a Hemisphere Protuberance,'' J. Fluid Mech., **175**, pp. 1–41.
[52] Keynton, R. S., Evancho, M. M., Sims, R. L., Rodway, N. V., Gobin, A., and Rittgers, S. E., 2001, ''Intimal Hyperplasia and Wall Shear in Arterial Bypass Graft Distal Anastomoses: An *In Vivo* Model Study,'' J. Biomech. Eng., **123**, pp. 464–73.